ACS OMEGA

Open Access

http://pubs.acs.org/journal/acsodf

Article

Exploring the Phase Stability of $Li_2Mn_{1-x}TM_xO_3$ (TM = Ni, Co, Cr, Ru) Cathode Materials in Lithium-Ion Batteries via the Cluster Expansion Method

Mamonamane Gratitude Mphahlele, Mallang Cliffton Masedi, Kemeridge Tumelo Malatji, Phuti Esrom Ngoepe, and Raesibe Sylvia Ledwaba*

Cite This: *ACS Omega* 2024, 9, 23400−23409

Read Online

ACCESS | Metrics & More | Article Recommendations | Supporting Information

ABSTRACT: Li_2MnO_3 has garnered significant interest as a potential cathode material due to its high electrochemical capacity, cost-effectiveness, and eco-friendliness. Nonetheless, its practical utilization is hindered by structural deterioration, which results in rapid capacity and voltage decay during cycling. To mitigate these challenges, cationic dopants have been incorporated to minimize structural collapse and enhance cathode material performance. Consequently, there is a strong desire to identify novel doped configurations as a remedial strategy for optimizing Li_2MnO_3 properties. In this study, the stability of the $Li_2Mn_{1-x}TM_xO_3$ system (TM = Ni, Co, Cr, Ru) was explored using cluster expansion and Monte Carlo simulations. By employing cluster expansion, binary ground state diagrams were generated, revealing 73, 65, 90, and 83 newly stable phases in $Li_2Mn_{1-x}Ni_xO_3$, $Li_2Mn_{1-x}Co_xO_3$, $Li_2Mn_{1-x}Cr_xO_3$, and $Li_2Mn_{1-x}Ru_xO_3$, respectively. The outcomes indicated that $Li_2Mn_{0.83}Ni_{0.17}O_3$, $Li_2Mn_{0.5}Co_{0.5}O_3$, $Li_2Mn_{0.5}Cr_{0.5}O_3$, and $Li_2Mn_{0.5}Ru_{0.5}O_3$ represent the most stable doped phases within the Li_2MnO_3 system. The application of Monte Carlo simulations enabled the assessment of high-temperature characteristics across the entire range of TM concentrations ($0 \le x \le 1$), facilitating the construction of phase diagrams. The $Li_2Mn_{1-x}Ni_xO_3$, $Li_2Mn_{1-x}Co_xO_3$, $Li_2Mn_{1-x}Cr_xO_3$, and $Li_2Mn_{1-x}Ru_xO_3$ systems exhibited favorable mixing at temperatures of 850, 700, 1700, and 1300 K, respectively. These discoveries present a clear trajectory for optimizing the properties of Li_2MnO_3, offering valuable insights into conceptualizing innovative cathode materials characterized by enhanced stability and performance.

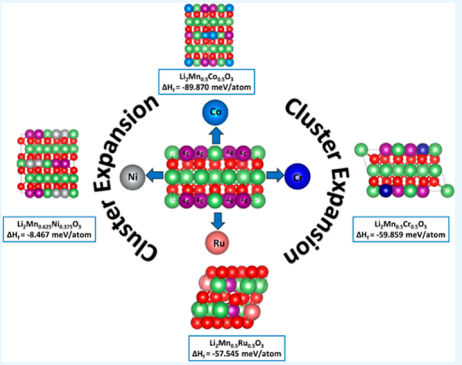

1. INTRODUCTION

Cluster expansion (CE) is a well-established technique extensively employed to investigate the properties that depend on the arrangement of components in alloyed systems.[1−7] The essence of CE is to depict the properties of systems that vary based on configuration by expressing them as a summation of bonds. In CE, these bonds are denoted as clusters, and the relationship between properties and configuration is established by summing cluster functions, with coefficients represented as effective cluster interactions (ECIs).[1] This representation is theoretically precise when accounting for all potential clusters, but this approach becomes unfeasible due to

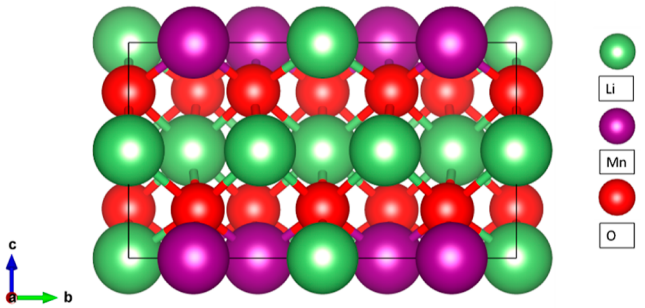

Figure 1. Crystalline structure of layered Li_2MnO_3.

Table 1. Equilibrium Lattice Parameters and Heats of Formation of Bulk Li_2MnO_3

structure	lattice parameters (Å)		ΔH_f (eV)	volume (Å^3)
	this work	exp[49]		
Li_2MnO_3	a = 4.984	4.937	−9.063	11.415
	b = 8.612	8.532		
	c = 5.065	5.030		

Received: December 25, 2023
Revised: March 5, 2024
Accepted: March 8, 2024
Published: May 22, 2024

its impracticality. In practice, cluster sets are truncated, and CE yields the same outcome. This study mainly focuses on the total energy of $Li_2Mn_{1-x}TM_xO_3$ $(0 \leq x \leq 1)$ occupation configurations in their relaxed structures. With a selected set of clusters, ECIs are typically determined by adjusting the energies of various configurations calculated using density functional theory techniques.

The continued interest in the CE method underscores its methodological complexity and ongoing relevance,[8−10] particularly in light of the resurgence of machine learning (ML) techniques.[11] A primary challenge faced by researchers across various statistical learning problems, including materials research, is the creation of accurate, unbiased, and low-variance models with limited data sets, often derived from computationally intensive first-principles calculations.[12] While traditional methods like ordinary least-squares regression have their merits, they often fall short, necessitating the development of sophisticated strategies to address issues such as model selection and systematic training set generation.[13−17]

In addition to employing predictive techniques common in ML, it is crucial to establish criteria for evaluating the accuracy of fitting, which ultimately aids in selecting the most suitable model. Model selection essentially becomes a form of statistical algorithm selection. One widely used strategy for this purpose is cross-validation (CV). The fundamental concept of CV involves dividing the data into segments, allowing for the estimation of the performance of each algorithm: a portion of the data (the training sample) is utilized to train each algorithm, while the remainder (the validation sample) is used to assess the algorithm's performance. Subsequently, CV identifies the algorithm with the lowest estimated risk. Various approaches to CV scoring exist, such as *k*-fold CV, leave-one-out validation, leave-p-out, balanced incomplete CV, Monte Carlo (MC) CV, and bias-corrected leave-one-out bootstrap, among others. Detailed discussions on CV procedures are available in the literature.[18] In the context of this study, the leave-many-out approach of CV scoring is employed to evaluate how well the energies of structures within a given training set compare to one another in a CE[19,20]

Researchers are increasingly leveraging data-driven ML techniques to drive the discovery and design of novel materials with superior properties,[21] leveraging the abundance of materials data available in databases like materials project,[22] AFLOWlib,[23] and Open Quantum Materials Database.[24] However, constructing precise ML models poses significant challenges due to the complex nature of material problems and model sensitivity to hyperparameters. In response, automated machine learning has emerged as a promising avenue, with innovations like Auto-MatRegressor[25] specifically tailored for materials property prediction. This approach streamlines model construction through meta-learning, collaborative recommendation, and hyperparameter optimization, enhancing usability and reliability in materials research.

In materials science, generative artificial intelligence (GAI) presents both opportunities and challenges. Ensuring high-quality data representation and effective integration of domain knowledge is essential for improving data quality and aligning generated samples with scientific principles. Moreover, enhancing the generalization ability of GAI models, improving interpretability and credibility, streamlining usability, and addressing security vulnerabilities are crucial steps toward safeguarding GAI models' integrity and reliability in materials science applications.[26]

In materials science, CE is often applied to pipelining calculation models that aim to estimate the materials' properties. It is usually used by combining first-principles calculations and MC simulations to investigate materials' thermodynamics and kinetics. This approach employs supercells containing millions of atoms to closely approximate reality.[27] The early application of CE was by Sanchez and de Fontaine[28] to predict ordered superstructures in metallic alloys, in which they investigated the impact of configurational entropy in binary alloys. de Fontaine used the CE method to construct the phase diagram of Ti−Rh and the O-order phase diagram of YBauCuO. A study by van der Ven[29] employed the CE formalism to characterize the configurational dependence of activation barriers and analyze the lithium diffusion mechanisms in Li−Co−O systems. Their findings indicated that in Li_xCoO_2, Li diffusion was facilitated by pairs of vacancies at all Li concentrations. Additionally, they projected significant variations in diffusion coefficients with Li concentration due to a pronounced concentration-dependent activation barrier. Arroyo-de Dompablo[30] constructed a phase diagram of the Li_xNiO_2 system using FP-MC calculations, wherein energy dependence of the Li-vacancy configurational disorder was parametrized using the CE. This study revealed distinct behavior between Li_xNiO_2 and Li_xCoO_2, despite having the same host structures and similar ionic radii for Ni and Co. Yang et al. employed FPMC to explore the arrangement of $Li_xLa_{(1-x)/3}NbO_3$, a site-deficient perovskite material that exhibits structure dependent ionic conductivity. The study found two plausible modulated systems for the La-rich layers responsible for lower-than-expected conductivity.[31]

In the pursuit of higher energy densities for lithium-ion batteries (LIBs) in various applications, the limited capacity of current cathode materials remains a constraining factor. This study will use the CE technique to generate doped Li_2MnO_3. The Li_2MnO_3 is a layered material which has received wide attention as a potential cathode material due to its superior capacity, low cost and environmental benignity.[32] Although this layered material is advantageous in terms of commercial availability, its flaws limit its practical application. The electrochemical activation process of Li_2MnO_3 that occurs at about 4.5 V is accompanied by lattice oxygen redox, contributing considerable additional capacity. However, the irreversible free oxygen release and the migration of transition metal ions lead to reduced Coulombic efficiency and poor cycle stability, which restricts their viability for widespread commercial use.[33,34] Therefore, it is imperative to modify this article to address these problems. Different methods have been contemplated to enhance the structural and electrochemical aspects of the Li_2MnO_3 electrode. The doping strategy has been shown to be the most effective in addressing these issues. This work selected four transition metals, Ni, Co, Ru and Cr, for doping Li_2MnO_3 at the Mn site. Extensive research has been done on the doping of Ni,[35−40] Co,[39−41] Ru,[38,40,42] and Cr[41,43,44] into LMO. A density functional theory (DFT) + U study presented by Lanjan et al.[39] showed that replacing 50% Mn with Ni or Co reduces the band gap and consequently increases the conductivity of $Li_2Mn_{0.5}TM_{0.5}O_3$. This study further demonstrated that introducing these dopants stabilizes $Li_2Mn_{0.5}TM_{0.5}O_3$ by preventing the spontaneous removal of oxygen during charge/discharge, thus making the material safer to use. Moreover, a DFT study by Kong et al.[45] illustrated that structures of Li_2MnO_3 doped with Ni, Ru or Co are thermodynamically stable with positive heats of formation.

https://doi.org/10.1021/acsomega.3c10357
ACS Omega 2024, 9, 23400−23409

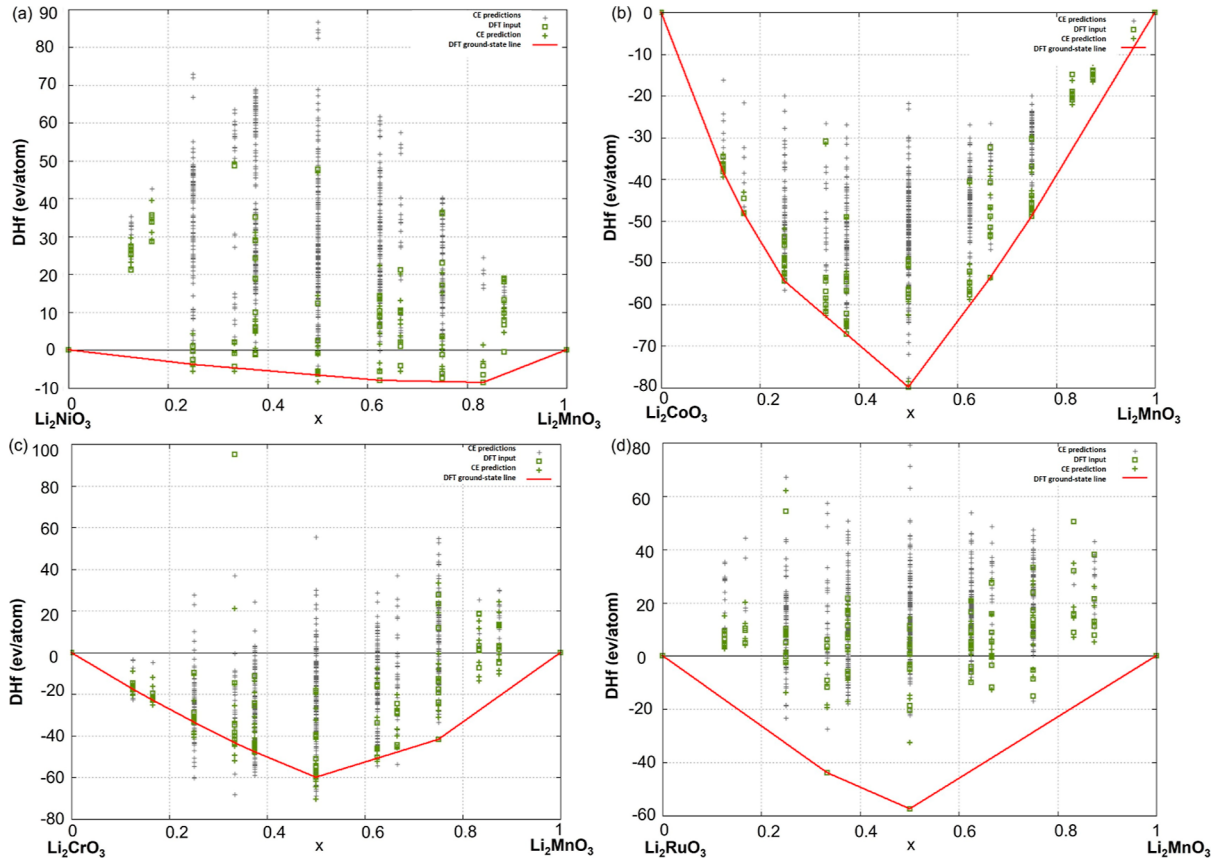

Figure 2. Binary diagrams of $Li_2Mn_{1-x}TM_xO_3$ where TM is (a) Ni, (b) Co, (c) Cr, and (d) Ru.

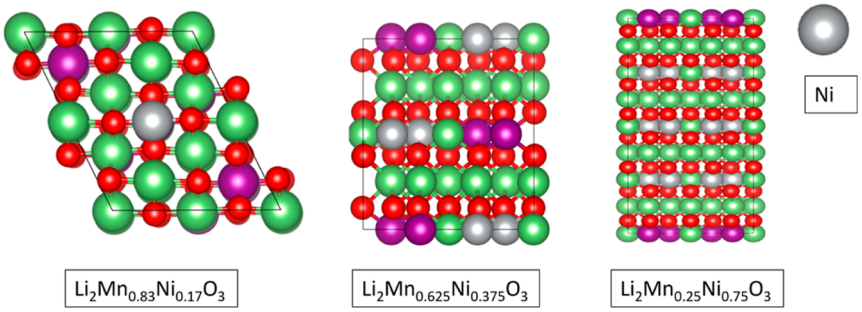

Figure 3. Structures of $Li_2Mn_{1-x}Ni_xO_3$ along the red ground state diagram.

Additionally, they observed that Ni and Ru doping not only curbs the formation of electron polarons but also enhances conductivity. Mori et al.[46] introduced Ru to Li_2MnO_3. They observed that $Li_2Mn_{0.4}Ru_{0.6}O_3$ exhibited an initial cycle discharge capacity of 192 mAh/g and retained approximately 88% of the primal capacity after 10 cycles at 0.1 C. Exploring various transition metal elements for dopants to substitute some Mn ions, Kim et al.[47] found that substituting 1% of Mn ions with Cr in Li_2MnO_3 resulted in a significantly elevated initial discharge capacity of 234.9 mAh/g, surpassing the pristine material. However, the capacity retention ratio was only 72% after 10 cycles at a lower current density of 0.05 C. In an experimental study involving Ni doping conducted by Lee's group,[37] redox reactions and prolonged cycling with reduced voltage decay were observed. These literature findings demonstrate a significant gap in exploring all of the possible combinations for a wide range of TM-doped structures and effectively attaining thermodynamically stable phases. Having established doping Li_2MnO_3 with transition metals appears to be the most effective strategy, opening room for a thorough exploration of this doped cathode materials. As such, the current work employs state-of-the-art ML techniques to generate new thermodynamically stable phases with varying symmetries and concentrations as a corrective measure to address the challenges encountered with pristine Li_2MnO_3. MC simulations will explore the thermodynamic behavior based on the output CE models. Furthermore, X-ray diffraction (XRD) analysis will be employed to characterize the most stable phases. While this paper focused on the application of the CE method to analyze the properties of $Li_2Mn_{1-x}TM_xO_3$ materials, future research will explore the complementary approach of group-subgroup transformation.[48] The group-subgroup transformation method involves reducing the symmetry of the parent structure to generate possible ordered phases of electrolytes or electrodes with variable concentrations of mobile ions. By employing lattice transformation

https://doi.org/10.1021/acsomega.3c10357
ACS Omega 2024, 9, 23400−23409

Table 2. Stable Structures of $Li_2Mn_{1-x}Ni_xO_3$ along the Ground State Line

structure	space group	a (Å)	b (Å)	c (Å)	ΔH_f (meV/atom)
Li_2NiO_3	$C2/m$	4.866	8.424	4.982	0.0000
$Li_2Mn_{0.83}Ni_{0.17}O_3$	$C2$	9.662	8.587	8.180	−8.467
$Li_2Mn_{0.625}Ni_{0.375}O_3$	$C2$	12.613	8.546	9.883	−7.969
$Li_2Mn_{0.25}Ni_{0.75}O_3$	$C2/m$	4.889	8.478	18.943	−3.694

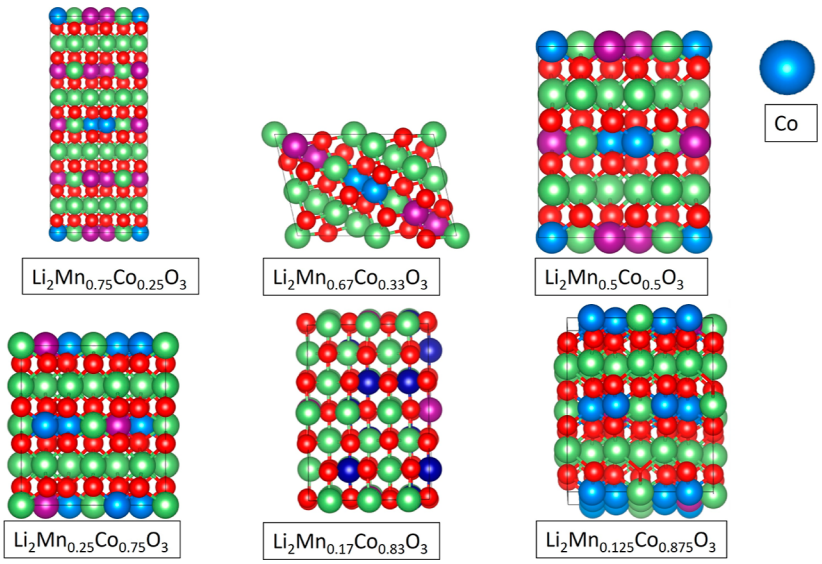

Figure 4. Structures of $Li_2Mn_{1-x}Co_xO_3$ along the red ground state diagram.

Table 3. Stable Structures of $Li_2Mn_{1-x}Co_xO_3$ along the Ground State Line

structure	space group	a (Å)	b (Å)	c (Å)	ΔH_f(meV/atom)
Li_2CoO_3	$C2/m$	4.904	8.483	5.007	0.000
$Li_2Mn_{0.75}$ $Co_{0.25}O_3$	$C2/c$	19.147	8.572	4.967	−49.749
$Li_2Mn_{0.67}Co_{0.33}O_3$	$P\bar{1}$	9.937	6.448	4.960	−64.622
$Li_2Mn_{0.5}Co_{0.5}O_3$	$C2/c$	9.641	8.528	4.947	−89.870
$Li_2Mn_{0.25}Co_{0.75}O_3$	$C2/c$	9.518	8.515	9.873	−64.446
$Li_2Mn_{0.17}Co_{0.83}O_3$	$C2$	4.967	8.482	5.739	−48.141
$Li_2Mn_{0.125}Co_{0.875}O_3$	$C2$	12.580	8.483	9.820	−38.184

Table 4. Stable Structures of $Li_2Mn_{1-x}Cr_xO_3$ along the Ground State Line

structure	space group	a (Å)	b (Å)	c (Å)	ΔH_f (meV/atom)
Li_2CrO_3	$C2/m$	5.063	8.750	5.105	0.000
$Li_2Mn_{0.75}Cr_{0.25}O_3$	$C2$	9.696	8.623	10.006	−42.675
$Li_2Mn_{0.67}Cr_{0.33}O_3$	$P\bar{1}$	7.686	7.686	5.822	−50.337
$Li_2Mn_{0.5}Cr_{0.5}O_3$	$P\bar{1}$	8.681	5.073	4.993	−59.859
$Li_2Mn_{0.375}Cr_{0.625}O_3$	$P1$	6.487	7.741	8.657	−47.942
$Li_2Mn_{0.33}Cr_{0.67}O_3$	$P\bar{1}$	12.669	5.095	4.990	−43.320
$Li_2Mn_{0.25}Cr_{0.75}O_3$	$P\bar{1}$	8.745	7.745	6.480	−33.698
$Li_2Mn_{0.17}Cr_{0.83}O_3$	$C2$	15.040	8.725	5.085	−22.988
$Li_2Mn_{0.125}Cr_{0.875}O_3$	$C2$	9.726	8.659	10.092	−17.468

and Wyckoff-position splitting, the group-subgroup transformation method allows for the formulation of ordered phases and the determination of stable ordered ground states. Investigating this method will provide further insights into predicting ordered phases in rechargeable battery materials, expanding upon the findings presented in this study.

The structure of Li_2MnO_3 is described by space group $C2/m$ in a monoclinic cell, as shown in Figure 1. The lattice parameters of the system used in this study and the experimental values are listed in Table 1. The lithium ions occupy the 2b (0, 1/2, 0), 2c (0, 0, 1/2), and 4h (0, 0.6606, 1/2) sites, the manganese ions the 4g (0, 0.16708, 0) site, and the oxygen ions the 4i (0.2189, 0, 0.2273) and 8j (0.2540, 0.32119, 0.2233) sites. It has an O_3-type structure, which can be redefined as $Li[Li_{1/3}Mn_{2/3}]O_2$. The transitional metal layer comprises monovalent lithium and tetravalent manganese with Li and Mn ions occupying octahedral sites in a 1:2 ratio. The lithium and transition metal layers are alternately arranged.[49]

https://doi.org/10.1021/acsomega.3c10357
ACS Omega 2024, 9, 23400−23409

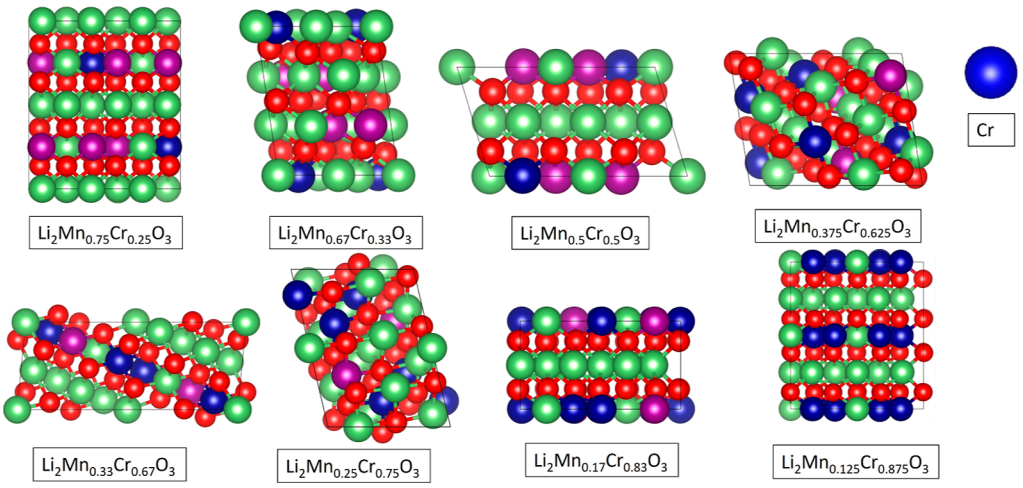

Figure 5. Structures of $Li_2Mn_{1-x}Cr_xO_3$ along the red ground state diagram.

2. RESULTS AND DISCUSSION

This section captures the study results, which aimed to generate $Li_2Mn_{1-x}TM_xO_3$ using the CE technique and subsequently to explore these generated systems at finite temperatures using MC simulations.

Table 5. Stable Structures of $Li_2Mn_{1-x}Ru_xO_3$ along the Ground State Line

structure	space group	a (Å)	b (Å)	c (Å)	ΔH_f (eV/atom)
Li_2RuO_3	$C2/m$	5.214	8.379	5.258	0.000
$Li_2Mn_{0.5}Ru_{0.5}O_3$	$P\bar{1}$	5.910	7.753	4.955	−57.545
$Li_2Mn_{0.33}Ru_{0.67}O_3$	$P\bar{1}$	5.925	11.415	4.884	−43.760

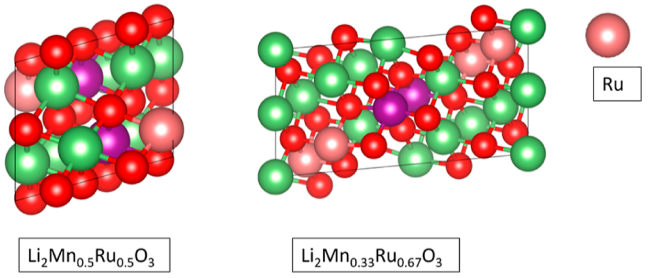

Figure 6. Structures of $Li_2Mn_{1-x}Ru_xO_3$ along the red ground state diagram.

2.1. Ground State Structures of $Li_2Mn_{1-x}TM_xO_3$. Binary phase diagrams were generated during the CE of the predictions of $Li_2Mn_{1-x}TM_xO_3$ structures, and the diagrams are presented by plotting their enthalpies of formation versus the transition metal concentration x. The green squares represent DFT enthalpies of formation of the training set, green crosses CE predicted enthalpies of formation of the training set and gray the CE predicted enthalpies of formation of all other structures considered by the CE. The most stable phase is characterized by the lowest enthalpy of formation, and negative enthalpy implies that the structure can be realistically achieved through experimental methods. It is essential to acknowledge that the calculated heat of formation is based on a temperature of 0 K. However, arrangements with disordered TM/Mn atoms may acquire stability in an unstable configuration by introducing mixing entropy and lattice vibrations at elevated temperatures.

Figure 2 shows a binary ground state diagram of the $Li_2Mn_{1-x}TM_xO_3$ system. Illustrated as Figure 2a is the ground state diagram of $Li_2Mn_{1-x}Ni_xO_3$, adapted from previous work,[50] that the system has generated 73 new structures in the negative and positive heats of formation, the structures are listed in Table S1 along with their space groups and formulas. The summary of the iterative optimization progress is shown in Table S2. The graph additionally demonstrates that the system favors phases with lower nickel content. The system reaches greater stability around $X = 0.2$.

Presented in Figure 2b, the ground state diagram of the $Li_2Mn_{1-x}Co_xO_3$ system shows all 65 generated miscible constituents at $T = 0$ K, listed in Table S3; that is, all phases are in the negative heats of formation. The iterative process is summarized in Table S4, the fifth column stayed vacant, indicating that the model did not transition to a state of miscibility gap, and the optimization process using CE concluded successfully with a CV score of 1.6 meV/pos. The most stable structure configuration is located at $x = 0.5$.

Figure 2c presents a binary ground state diagram of the $Li_2Mn_{1-x}Cr_xO_3$ system. The CE generated 90 phases listed in Table S5, of which 10 are on the ground state diagram. The diagram further illustrates that the most stable configuration is also at $x = 0.5$. As indicated in Table S6, the CE reached convergence with a CV score of 16.0 meV per atomic position.

Lastly, the binary ground state diagram of $Li_2Mn_{1-x}Ru_xO_3$ in Figure 2d produced 83 new structures, from which only 4 structures are on the DFT ground-state line. The structures are shown in Table S7. The most stable phase is identified at $x = 0.5$. As depicted in Table S8, the optimization of the CE concluded successfully, achieving a CV score of 8.5 meV per position in the final iteration. These diagrams collectively offer valuable insights into the thermodynamic stability and structural configurations of the $Li_2Mn_{1-x}TM_xO_3$ system across various transition metal concentrations.

2.1.1. Structural Properties of Stable $Li_2Mn_{1-x}TM_xO_3$ Phases along the Ground State Line. As mentioned, the most important structures lie along the ground state line. The structures of $Li_2Mn_{1-x}Ni_xO_3$ that are on the ground state line are shown in Figure 3, and their properties are listed in Table 2. CE predicted $Li_2Mn_{0.83}Ni_{0.17}O_3$ with space group $C2$ as the

https://doi.org/10.1021/acsomega.3c10357
ACS Omega 2024, 9, 23400−23409

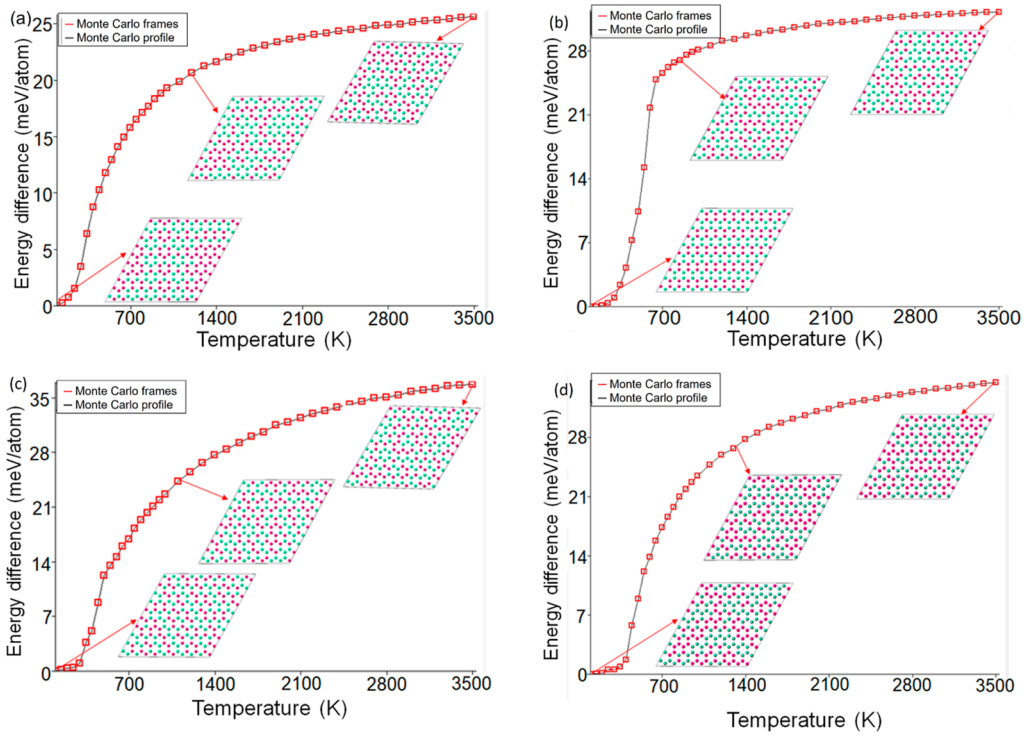

Figure 7. Temperature profiles cross sections through the 10 × 10 × 10 MC simulation cells of (a) $Li_2Mn_{0.5}Ni_{0.5}O_3$, (b) $Li_2Mn_{0.5}Co_{0.5}O_3$, (c) $Li_2Mn_{0.5}Cr_{0.5}O_3$, and (d) $Li_2Mn_{0.5}Ru_{0.5}O_3$.

most thermodynamically stable structure, with the lowest heat of formation.

In Figure 4, all 8 structures of $Li_2Mn_{1-x}Co_xO_3$ along the ground state line are presented. The monoclinic structure $Li_2Mn_{0.5}Co_{0.5}O_3$, characterized by the space group $C2/c$, was identified as the most thermodynamically stable among them. A detailed listing of the properties of these phases can be found in Table 3.

Table 4 lists all the phases along the ground state line and their respective formation energies. The structures of these phases are visually depicted in Figure 5. The most stable phase is triclinic $Li_2Mn_{0.5}Cr_{0.5}O_3$ with space group $P\bar{1}$.

Table 5 presents the most stable structures, their space groups, and their formation energies. The most stable phase was triclinic $Li_2Mn_{0.5}Ru_{0.5}O_3$ with space group $P\bar{1}$ the structures are shown in Figure 6.

2.2. Thermodynamic Properties. *2.2.1. Temperature Profiles.* In this section, we delve into the high-temperature properties of the studied systems, employing MC simulations based on the Metropolis algorithm.[51] MC simulations serve as a powerful tool for probing the thermodynamic and kinetic properties of materials with a specific focus in this study on the analysis of phase transitions and phase diagrams. The code performs simulations within either the canonical or the grand canonical ensemble. The canonical ensemble was chosen for the MC simulation of the $Li_2Mn_{1-x}TM_xO_3$ systems. The decision to employ the canonical ensemble in the MC simulation of the $Li_2Mn_{1-x}TM_xO_3$ systems was driven by the systems' nature. These systems were considered closed, meaning they had a fixed and predetermined number of particles. All the systems used periodic cells with 12,000 atoms. The temperature was varied from 0 to 3500 K for all the systems. Temperature profiles for $Li_2Mn_{1-x}Ni_xO_3$, $Li_2Mn_{1-x}Co_xO_3$, $Li_2Mn_{1-x}Cr_xO_3$, and $Li_2Mn_{1-x}Ru_xO_3$ showing phase changes across different concentrations are shown below.

Figure 7 illustrates the changes in energies per atom and the corresponding level of inversion within $Li_2Mn_{0.5}TM_{0.5}O_3$ configurations over a temperature range spanning from 0 to 3500 K. These variations were determined through MC simulation. The diagram also presents snapshots of the structures generated at different temperatures. The energy gap between these configurations consistently widens as temperature increases, with a sudden reduction in the rate of this increase occurring around the critical temperature. This transition coincides with the initiation of reverse inversion. Below the critical temperature, the introduced TM element separates to form precipitates, indicating the solubility limits for Li_2MnO_3. For visualization purposes, the O and Li were removed; pink spheres denote the transition metal dopant, while manganese is represented by green.

2.2.2. Phase Diagrams. In this section, phase diagrams are computed from concentrations of manganese and TM = Ni, Co, Cr, and Ru with critical temperatures generated from the MC interactive temperature versus energy graphs above and are shown in Figure 8. These phase diagrams can be used to predict the phase changes in a material after being subjected to a specific heat treatment process. This holds importance as the characteristics of the constituents of a material are dictated by the phases present within the material.

Figure 8a,b,d shows two cooling curves. The phase separation decreases as the system is cooled. Inside the curves, the systems are phase separating, and the mixture of two phases of Li_2MnO_3 and Li_2TMO_3 is stable. Beyond the curve, the stability of single-phase, uniform $Li_2Mn_{1-x}TM_xO_3$ is maintained. The temperatures at which mixing occurs are 850, 700, and 1300 K for $Li_2Mn_{1-x}Ni_xO_3$, $Li_2Mn_{1-x}Co_xO_3$, and $Li_2Mn_{1-x}Ru_xO_3$, respectively. The depiction of the miscibility

https://doi.org/10.1021/acsomega.3c10357
ACS Omega 2024, 9, 23400−23409

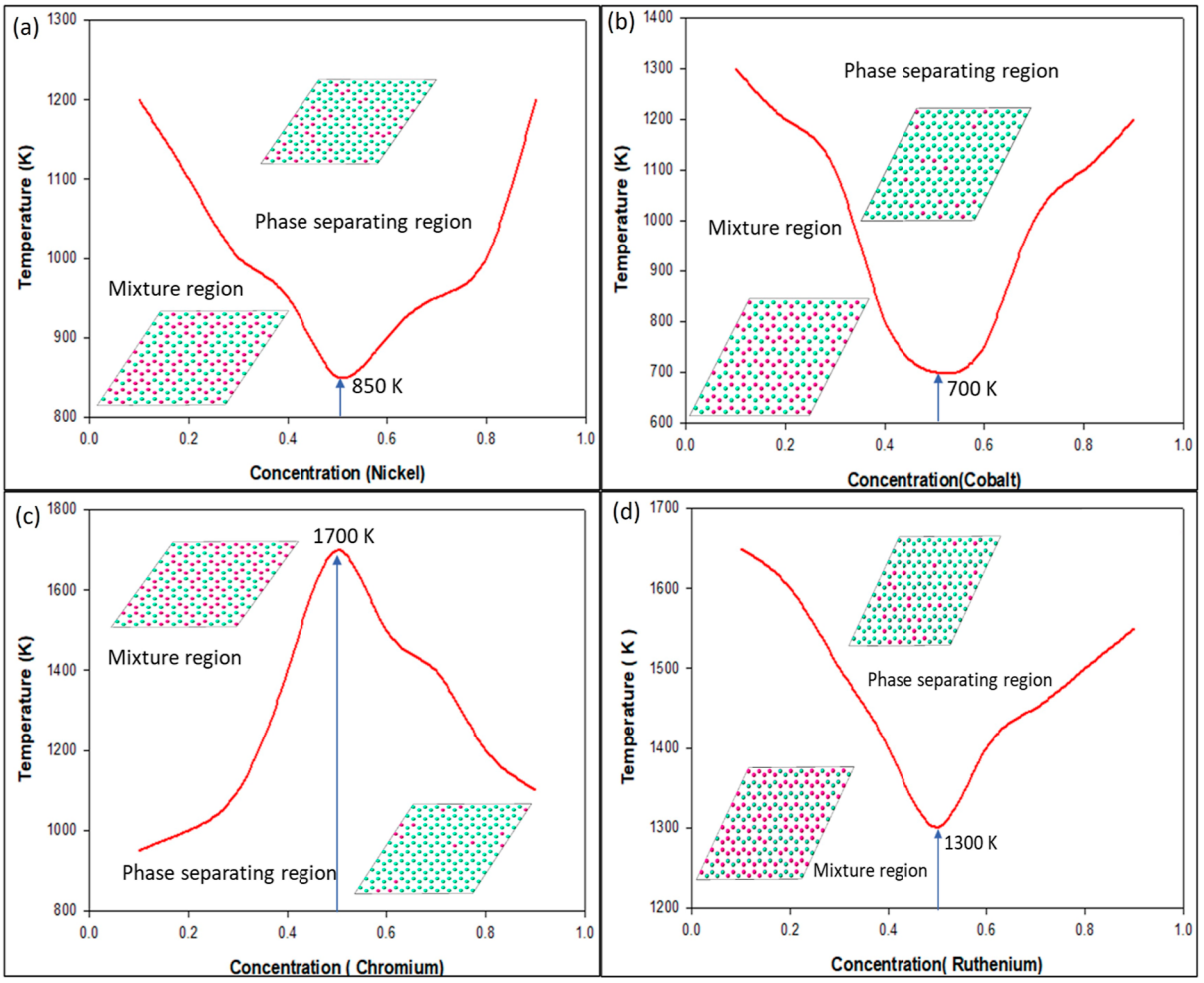

Figure 8. Constructed phase diagram of (a) $Li_2Mn_{1-x}Ni_xO_3$, (b) $Li_2Mn_{1-x}Co_xO_3$, (c) $Li_2Mn_{1-x}Cr_xO_3$, and (d) $Li_2Mn_{1-x}Ru_xO_3$ using the critical temperature at different concentrations.

gap for $Li_2Mn_{1-x}Cr_xO_3$ is presented in Figure 8c. As the temperature rises, this gap diminishes—the two phases mix at the highest point of the curve, at 1700 K.

2.3. XRD. The XRD analysis examined the degree of crystallinity in the phases under investigation. The peak width observed in the analysis is inversely correlated to the size of the crystals. A narrower peak indicates larger crystals, while a broader peak could imply the presence of smaller crystals, defects, or the potential for the systems to be either amorphous or solid with imperfect crystalline structures. The XRD patterns for various $Li_2Mn_{1-x}Tm_xO_3$, systems have been illustrated in Figure 9a−d. Notably, all systems exhibit well-defined peaks, indicating a high level of crystallinity within the phases. All XRDs of Li_2TMO_3 have weak peaks between 20 and 25° and (001) at ∼20°, consistent with monoclinic $C2/m$ symmetry. Additionally, splitting peaks around 65° suggest a layered structure for these systems, a characteristic feature observed consistently, even in the most stable doped phase.[52]

3. MATERIALS AND METHODS

In this section, we discuss the method used to generate $Li_2Mn_{1-x}TM_xO_3$ and the working scheme of the code used.

3.1. Cluster Expansion. A CE technique[53] describes cluster functions as an orthogonal basis for a multidimensional space of discrete spin variables. This technique indicates that an Icing-like Hamiltonian for the energies of various atomic configurations. For implementing the CE approach, the Universal Cluster Expansion code (UNCLE)[54] was used owing to its ability to manage most of the activities involved in calculating the thermodynamic properties of the CE Hamiltonian. The UNCLE code was to identify the thermodynamically stable phases of $Li_2Mn_{1-x}TM_xO_3$ within the whole range of $0 \leq x \leq 1$; the UNCLE program is applied at a series of Mn/TM ratios via the MedeA package. This method is based on the standard CE formalism coupled with the ground-state configuration search and the DFT structure relaxations.[1]

The code determines stable multicomponent crystal structures and ranks metastable structures by the enthalpy of formation while maintaining the predictive power and accuracy of density functional methods. The ground-state binary phase diagrams encompassing various structures with different concentrations and symmetries were generated for transition-metal-doped Li_2MnO_3 systems.

The fitting scheme was iterated 10 times for all systems, with a maximum of 5 structures added in each iteration. The initial training set consisted of 5 structures. The iterations continued until the energies predicted by the CE surpassed the energy computed for the structure on the ground-state line at each sampled concentration.

3.2. Monte Carlo Simulations. The MC simulations[55] were performed under a canonical ensemble using the UNLCE

https://doi.org/10.1021/acsomega.3c10357
ACS Omega 2024, 9, 23400−23409

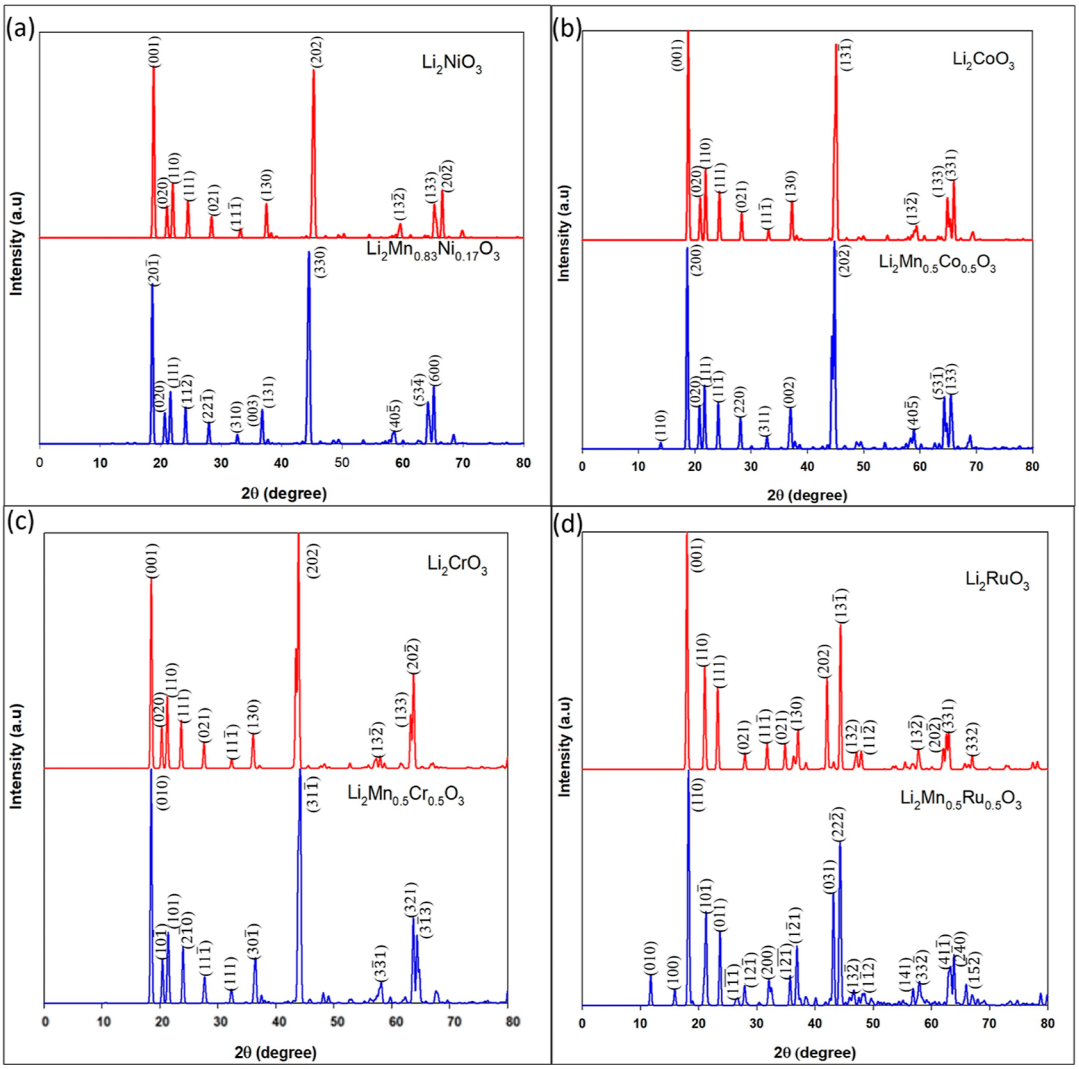

Figure 9. XRD patterns of (a) $Li_2Mn_{1-x}Ni_xO_3$, (b) $Li_2Mn_{1-x}Co_xO_3$, (c) $Li_2Mn_{1-x}Cr_xO_3$ and (d) $Li_2Mn_{1-x}Ru_xO_3$.

code for finite temperature studies. The code applied for studying the thermodynamics properties is a simple Metropolis algorithm,[51] allowing the flipping of Mn and TM atoms in arbitrary distance mutual with the aim to reach the equilibrium configurations as fast as possible. The system randomly selects a pair of Mn and TM atoms and then calculates the energy difference caused by the exchange of the two atoms. The MC simulation was used to calculate the coherent phase boundaries of various phase diagrams. The MC simulations were carried out for different concentrations x, and the resultant critical temperature values were used to construct the coherent phase boundary of the systems. A 10 × 10 × 10 supercell was used with an initial temperature of 0 K and a final temperature of 3500 K with 100 K increments in a canonical ensemble. The number of steps to average over was 300,000 steps, and the convergence accuracy of the energy was set to 0.0001 eV. The averaging times for the given precision on the average concentration of the systems were set to 0.1% in the current simulations.

4. CONCLUSIONS

This work used the CE method combined with MC simulations to study $Li_2Mn_{1-x}TM_xO_3$ systems. The CE generated 73, 65, 90, and 83 new phases of $Li_2Mn_{1-x}Ni_xO_3$, $Li_2Mn_{1-x}Co_xO_3$, $Li_2Mn_{1-x}Cr_xO_3$, and $Li_2Mn_{1-x}Ru_xO_3$, respectively. The findings predict $Li_2Mn_{0.83}Ni_{0.17}O_3$, $Li_2Mn_{0.5}Co_{0.5}O_3$, $Li_2Mn_{0.5}Cr_{0.5}O_3$, and $Li_2Mn_{0.5}Ru_{0.5}O_3$ as the most thermodynamically stable phases of doped Li_2MnO_3. MC simulations were used to study the systems at finite temperatures, and phase diagrams were constructed. The $Li_2Mn_{1-x}Ni_xO_3$, $Li_2Mn_{1-x}Co_xO_3$, $Li_2Mn_{1-x}Cr_xO_3$, and $Li_2Mn_{1-x}Ru_xO_3$ systems were found to be phase-separating at 0 K, and mixing occurs at 850, 700, 1700, and 1300, respectively. The XRD patterns confirmed the crystallinity of the phases. These results highlight the efficacy and utility of combining the CE method and MC simulations in the exploration of stable multicomponent materials. The predictive power of this approach offers valuable insights into the thermodynamic stability and phase behavior of doped Li_2MnO_3, paving the way for the discovery and design of novel materials for LIBs.

■ ASSOCIATED CONTENT

Supporting Information

The Supporting Information is available free of charge at https://pubs.acs.org/doi/10.1021/acsomega.3c10357.

Ground state enthalpies of formation as derived by DFT and CE for the $Li_2Mn_{1-x}Ni_xO_3$, $Li_2Mn_{1-x}Co_xO_3$,

https://doi.org/10.1021/acsomega.3c10357
ACS Omega 2024, 9, 23400−23409

$Li_2Mn_{1-x}Cr_xO_3$, and $Li_2Mn_{1-x}Ru_xO_3$ systems; and summary of the iterative optimization progress $Li_2Mn_{1-x}Ni_xO_3$, $Li_2Mn_{1-x}Co_xO_3$, $Li_2Mn_{1-x}Cr_xO_3$, and $Li_2Mn_{1-x}Ru_xO_3$ systems (PDF)

AUTHOR INFORMATION

Corresponding Author

Raesibe Sylvia Ledwaba − *Materials Modelling Centre, University of Limpopo, Sovenga 0727, South Africa;* orcid.org/0000-0001-5807-5177; Email: raesibe.ledwaba@ul.ac.za

Authors

Mamonamane Gratitude Mphahlele − *Materials Modelling Centre, University of Limpopo, Sovenga 0727, South Africa;* orcid.org/0000-0002-2233-1009

Mallang Cliffton Masedi − *Materials Modelling Centre, University of Limpopo, Sovenga 0727, South Africa*

Kemeridge Tumelo Malatji − *Materials Modelling Centre, University of Limpopo, Sovenga 0727, South Africa*

Phuti Esrom Ngoepe − *Materials Modelling Centre, University of Limpopo, Sovenga 0727, South Africa*

Complete contact information is available at: https://pubs.acs.org/10.1021/acsomega.3c10357

Author Contributions

M.G.M. performed the computational calculations and wrote this paper; R.S.L. contributed data analysis, review, editing, and supervised this work; M.C.M. and K.T.M. assisted with methodology, data analysis, and validation; P.E.N. contributed conceptualization, resources, and analysis. All authors have read and agreed to the published version of the manuscript.

Funding

The South African Research Chair Initiative (SARChI) of the Department of Science and Innovation (DSI) and the National Research Foundation (NRF) Grant number 133746 in Pretoria, the DSI Energy Storage Research Development Innovation initiative, funded this research.

Notes

The authors declare no competing financial interest.

ACKNOWLEDGMENTS

The authors acknowledge the Centre for High-Performance Computing (CHPC) in Cape Town for computing resources.

REFERENCES

(1) Sanchez, J. M.; Ducastelle, F.; Gratias, D. Generalized Cluster Description of Multicomponent Systems. *Physica A* **1984**, *128* (1−2), 334−350.

(2) Blum, V.; Zunger, A. Mixed-Basis Cluster Expansion for Thermodynamics of Bcc Alloys. *Phys. Rev. B* **2004**, *70* (15), 155108.

(3) Zarkevich, N. A.; Johnson, D. D. Reliable First-Principles Alloy Thermodynamics via Truncated Cluster Expansions. *Phys. Rev. Lett.* **2004**, *92* (25), 255702.

(4) Wolverton, C.; de Fontaine, D. Cluster Expansions of Alloy Energetics in Ternary Intermetallics. *Phys. Rev. B* **1994**, *49* (13), 8627−8642.

(5) Laks, D. B.; Ferreira, L. G.; Froyen, S.; Zunger, A. Efficient Cluster Expansion for Substitutional Systems. *Phys. Rev. B* **1992**, *46* (19), 12587−12605.

(6) Zhang, X.; Sluiter, M. H. F. Cluster Expansions for Thermodynamics and Kinetics of Multicomponent Alloys. *J. Phase Equilib. Diffus.* **2016**, *37* (1), 44−52.

(7) Diale, R. G.; Modiba, R.; Ngoepe, P. E.; Chauke, H. R. Phase Stability of $TiPd_{1-x}Ru_x$ and $Ti_{1-x}PdRu_x$ Shape Memory Alloys. *Mater. Today: Proc.* **2021**, *38*, 1071−1076.

(8) Cao, L.; Li, C.; Mueller, T. The Use of Cluster Expansions To Predict the Structures and Properties of Surfaces and Nanostructured Materials. *J. Chem. Inf. Model.* **2018**, *58* (12), 2401−2413.

(9) Kadkhodaei, S.; Muñoz, J. A. Cluster Expansion of Alloy Theory: A Review of Historical Development and Modern Innovations. *JOM* **2021**, *73* (11), 3326−3346.

(10) Eisenbach, M.; Pei, Z.; Liu, X. First-Principles Study of Order-Disorder Transitions in Multicomponent Solid-Solution Alloys. *J. Phys.: Condens. Matter* **2019**, *31* (27), 273002.

(11) Batra, R.; Song, L.; Ramprasad, R. Emerging Materials Intelligence Ecosystems Propelled by Machine Learning. *Nat. Rev. Mater.* **2020**, *6* (8), 655−678.

(12) Liu, Y.; Yang, Z.; Zou, X.; Ma, S.; Liu, D.; Avdeev, M.; Shi, S. Data Quantity Governance for Machine Learning in Materials Science. *Natl. Sci. Rev.* **2023**, *10* (7), nwad125.

(13) Nguyen, A. H.; Rosenbrock, C. W.; Reese, C. S.; Hart, G. L. W. Robustness of the Cluster Expansion: Assessing the Roles of Relaxation and Numerical Error. *Phys. Rev. B* **2017**, *96* (1), 014107.

(14) Leong, Z.; Tan, T. L. Robust Cluster Expansion of Multicomponent Systems Using Structured Sparsity. *Phys. Rev. B* **2019**, *100* (13), 134108.

(15) Kleiven, D.; Akola, J.; Peterson, A. A.; Vegge, T.; Chang, J. H. Training Sets Based on Uncertainty Estimates in the Cluster-Expansion Method. *J. Phys.: Energy* **2021**, *3* (3), 034012.

(16) Barroso-Luque, L.; Yang, J. H.; Ceder, G. Sparse Expansions of Multicomponent Oxide Configuration Energy Using Coherency and Redundancy. *Phys. Rev. B* **2021**, *104* (22), 224203.

(17) Shi, S.; Gao, J.; Liu, Y.; Zhao, Y.; Wu, Q.; Ju, W.; Ouyang, C.; Xiao, R. Multi-Scale Computation Methods: Their Applications in Lithium-Ion Battery Research and Development. *Chin. Phys. B* **2016**, *25* (1), 018212.

(18) Arlot, S.; Celisse, A. A Survey of Cross-Validation Procedures for Model Selection. *Stat. Surv.* **2010**, *4*, 40−79.

(19) Walle, A.; Ceder, G. Automating First-Principles Phase Diagram Calculations. *J. Phase Equilib.* **2002**, *23* (4), 348−359.

(20) Baumann, K. Cross-Validation as the Objective Function for Variable-Selection Techniques. *TrAC, Trends Anal. Chem.* **2003**, *22* (6), 395−406.

(21) Liu, Y.; Zhao, T.; Ju, W.; Shi, S. Materials Discovery and Design Using Machine Learning. *J. Materiomics* **2017**, *3* (3), 159−177.

(22) Jain, A.; Ong, S. P.; Hautier, G.; Chen, W.; Richards, W. D.; Dacek, S.; Cholia, S.; Gunter, D.; Skinner, D.; Ceder, G.; Persson, K. A. Commentary: The Materials Project: A Materials Genome Approach to Accelerating Materials Innovation. *APL Mater.* **2013**, *1* (1), 011002.

(23) Curtarolo, S.; Setyawan, W.; Hart, G. L. W.; Jahnatek, M.; Chepulskii, R. V.; Taylor, R. H.; Wang, S.; Xue, J.; Yang, K.; Levy, O.; Mehl, M. J.; Stokes, H. T.; Demchenko, D. O.; Morgan, D. AFLOW: An Automatic Framework for High-Throughput Materials Discovery. *Comput. Mater. Sci.* **2012**, *58*, 218−226.

(24) Saal, J. E.; Kirklin, S.; Aykol, M.; Meredig, B.; Wolverton, C. Materials Design and Discovery with High-Throughput Density Functional Theory: The Open Quantum Materials Database (OQMD). *JOM* **2013**, *65* (11), 1501−1509.

(25) Liu, Y.; Wang, S.; Yang, Z.; Avdeev, M.; Shi, S. Auto-MatRegressor: Liberating Machine Learning Alchemists. *Sci. Bull.* **2023**, *68* (12), 1259−1270.

(26) Liu, Y.; Yang, Z.; Yu, Z.; Liu, Z.; Liu, D.; Lin, H.; Li, M.; Ma, S.; Avdeev, M.; Shi, S. Generative Artificial Intelligence and Its Applications in Materials Science: Current Situation and Future Perspectives. *J. Materiomics* **2023**, *9* (4), 798−816.

(27) Wu, Q.; He, B.; Song, T.; Gao, J.; Shi, S. Cluster Expansion Method and Its Application in Computational Materials Science. *Comput. Mater. Sci.* **2016**, *125*, 243−254.

(28) Sanchez, J. M.; de Fontaine, D. 20—Theoretical Prediction of Ordered Superstructures in Metallic Alloys. *Ind. Chem. Libr.* **1981**, *2*, 117−132.
(29) Van der Ven, A.; Ceder, G.; Asta, M.; Tepesch, P. D. First-Principles Theory of Ionic Diffusion with Nondilute Carriers. *Phys. Rev. B* **2001**, *64* (18), 184307.
(30) Arroyo y de Dompablo, M. E.; Ceder, G. First-Principles Calculations on Li_xNiO_2: Phase Stability and Monoclinic Distortion. *J. Power Sources* **2003**, *119*−*121*, 654−657.
(31) Yang, Z.; Ward, R. E.; Tanibata, N.; Takeda, H.; Nakayama, M.; Asaka, T. Arrangement in $La_{1/3}NbO_3$ Obtained by First-Principles Density Functional Theory with Cluster Expansion and Monte Carlo Simulation. *J. Phys. Chem. C* **2020**, *124* (18), 9746−9754.
(32) Li, F.; Zhang, X.; Lin, J.; Ma, J.; Zhang, S.; Yang, G. Unveiling the Role of Oxygen Vacancy in Li_2MnO_3 upon Delithiation. *J. Phys. Chem. C* **2019**, *123* (38), 23403−23409.
(33) Armstrong, A. R.; Holzapfel, M.; Novák, P.; Johnson, C. S.; Kang, S.-H.; Thackeray, M. M.; Bruce, P. G. Demonstrating Oxygen Loss and Associated Structural Reorganization in the Lithium Battery Cathode $Li[Ni_{0.2}Li_{0.2}Mn_{0.6}]O_2$. *J. Am. Chem. Soc.* **2006**, *128* (26), 8694−8698.
(34) Wang, Z. Q.; Wu, M. S.; Xu, B.; Ouyang, C. Y. Improving the Electrical Conductivity and Structural Stability of the Li_2MnO_3 Cathode via P Doping. *J. Alloys Compd.* **2016**, *658*, 818−823.
(35) Matsunaga, T.; Komatsu, H.; Shimoda, K.; Minato, T.; Yonemura, M.; Kamiyama, T.; Kobayashi, S.; Kato, T.; Hirayama, T.; Ikuhara, Y.; Arai, H.; Ukyo, Y.; Uchimoto, Y.; Ogumi, Z. Structural Understanding of Superior Battery Properties of Partially Ni-Doped Li_2MnO_3 as Cathode Material. *J. Phys. Chem. Lett.* **2016**, *7* (11), 2063−2067.
(36) Ye, D.; Sun, C.; Chen, Y.; Ozawa, K.; Hulicova-Jurcakova, D.; Zou, J.; Wang, L. Ni-Induced Stepwise Capacity Increase in Ni-Poor Li-Rich Cathode Materials for High Performance Lithium Ion Batteries. *Nano Res.* **2015**, *8* (3), 808−820.
(37) Lee, J.; Gong, Y.; Gu, L.; Kang, B. Long-Term Cycle Stability Enabled by the Incorporation of Ni into Li_2MnO_3 Phase in the Mn-Based Li-Rich Layered Materials. *ACS Energy Lett.* **2021**, *6* (2), 789−798.
(38) Hoang, K. Doping Li-Rich Cathode Material Li_2MnO_3: Interplay between Lattice Site Preference, Electronic Structure, and Delithiation Mechanism. *Phys. Rev. Mater.* **2017**, *1* (7), 075404.
(39) Lanjan, A.; Ghalami Choobar, B.; Amjad-Iranagh, S. First Principle Study on the Application of Crystalline Cathodes $Li_2Mn_{0.5}TM_{0.5}O_3$ for Promoting the Performance of Lithium-Ion Batteries. *Comput. Mater. Sci.* **2020**, *173*, 109417.
(40) Kong, F.; Longo, R. C.; Yeon, D.-H.; Yoon, J.; Park, J.-H.; Liang, C.; KC, S.; Doo, S.-K.; Cho, K. First Principles Study of Li-Site Doping Effect on the Properties of $LiMnO_2$ and Li_2MnO_3 Cathode Materials. *ECS Trans.* **2015**, *64* (22), 21−32.
(41) Gao, Y.; Wang, X.; Ma, J.; Wang, Z.; Chen, L. Selecting Substituent Elements for Li-Rich Mn-Based Cathode Materials by Density Functional Theory (DFT) Calculations. *Chem. Mater.* **2015**, *27* (9), 3456−3461.
(42) Zhang, S.; Wang, J.; Tao, X.; Yan, X.; Du, Y.; Seifert, H. J.; Lei, T. Understanding the Different Effects of 4d-Transition Metals on the Performance of Li-Rich Cathode Li_2MnO_3 by First-Principles. *Phys. Chem. Chem. Phys.* **2023**, *25* (3), 2282−2293.
(43) Singh, G.; Thomas, R.; Kumar, A.; Katiyar, R. S. Electrochemical Behavior of Cr- Doped Composite Li_2MnO_3-$LiMn_{0.5}Ni_{0.5}O_2$ Cathode Materials. *J. Electrochem. Soc.* **2012**, *159* (4), A410−A420.
(44) Zhang, S.; Wang, J.; Liu, H.; Zhang, W.; Sun, L.; Du, Y.; Seifert, H. J.; Lei, T. Revealing the Different Effects of VIB Transition Metals X (X = Cr, Mo, W) on the Electrochemical Performance of Li-Rich Cathode Li_2MnO_3 by First-Principles Calculations. *Nanoscale* **2022**, *14* (40), 15034−15047.
(45) Kong, F.; Longo, R. C.; Park, M.-S.; Yoon, J.; Yeon, D.-H.; Park, J.-H.; Wang, W.-H.; KC, S.; Doo, S.-G.; Cho, K. Ab Initio Study of Doping Effects on $LiMnO_2$ and Li_2MnO_3 Cathode Materials for Li-Ion Batteries. *J. Mater. Chem. A* **2015**, *3* (16), 8489−8500.
(46) Mori, D.; Sakaebe, H.; Shikano, M.; Kojitani, H.; Tatsumi, K.; Inaguma, Y. Synthesis, Phase Relation and Electrical and Electrochemical Properties of Ruthenium-Substituted Li_2MnO_3 as a Novel Cathode Material. *J. Power Sources* **2011**, *196* (16), 6934−6938.
(47) Kim, S.; Noh, J.-K.; Yu, S.; Chang, W.; Chung, K. Y.; Cho, B.-W. Effects of Transition Metal Doping and Surface Treatment to Improve the Electrochemical Performance of Li_2MnO_3. *J. Electroceram.* **2013**, *30* (3), 159−165.
(48) Ran, Y.; Zou, Z.; Liu, B.; Wang, D.; Pu, B.; Mi, P.; Shi, W.; Li, Y.; He, B.; Lu, Z.; Lu, X.; Li, B.; Shi, S. Towards Prediction of Ordered Phases in Rechargeable Battery Chemistry via Group-Subgroup Transformation. *npj Comput. Mater.* **2021**, *7* (1), 184.
(49) Strobel, P.; Lambert-Andron, B. Crystallographic and Magnetic Structure of Li_2MnO_3. *J. Solid State Chem.* **1988**, *75* (1), 90−98.
(50) Mphahlele, M. G.; Masedi, M. C.; Malatji, K. T.; Ngoepe, P. E.; Ledwaba, R. S. The Effect of Ni-Doping on the Stability of Li_2MnO_3 Cathode Material: A DFT Study. *MATEC Web Conf.* **2023**, *388*, 07005.
(51) Metropolis, N.; Rosenbluth, A. W.; Rosenbluth, M. N.; Teller, A. H.; Teller, E. Equation of State Calculations by Fast Computing Machines. *J. Chem. Phys.* **1953**, *21* (6), 1087−1092.
(52) Kang, S.-H.; Kempgens, P.; Greenbaum, S.; Kropf, A. J.; Amine, K.; Thackeray, M. M. Interpreting the Structural and Electrochemical Complexity of $0.5Li_2MnO_3{\cdot}0.5LiMO_2$ Electrodes for Lithium Batteries ($M = Mn_{0.5-x}Ni_{0.5-x}Co_{2x}$, $0 \le x \le 0.5$). *J. Mater. Chem.* **2007**, *17* (20), 2069−2077.
(53) Müller, S. Bulk and Surface Ordering Phenomena in Binary Metal Alloys. *J. Phys.: Condens. Matter* **2003**, *15* (34), R1429−R1500.
(54) Lerch, D.; Wieckhorst, O.; Hart, G. L. W.; Forcade, R. W.; Müller, S. UNCLE: A Code for Constructing Cluster Expansions for Arbitrary Lattices with Minimal User-Input. *Modell. Simul. Mater. Sci. Eng.* **2009**, *17* (5), 055003.
(55) Binder, K.; Heermann, D. W.; Binder, K. *Monte Carlo Simulation in Statistical Physics*; Springer, 1992; Vol. *8*.

https://doi.org/10.1021/acsomega.3c10357
ACS Omega 2024, 9, 23400−23409